Journal of Power Sources 354 (2017) 215–228

Contents lists available at ScienceDirect

Journal of Power Sources

journal homepage: www.elsevier.com/locate/jpowsour

Thermal conductivity of catalyst layer of polymer electrolyte membrane fuel cells: Part 2 — Analytical modeling

Mohammad Ahadi [a], Andreas Putz [b], Jürgen Stumper [b], Majid Bahrami [a, *]

[a] Laboratory for Alternative Energy Conversion (LAEC), School of Mechatronic Systems Engineering, Simon Fraser University, Surrey, BC V3T 0A3, Canada
[b] Automotive Fuel Cell Cooperation, 9000 Glenlyon Parkway, Burnaby, BC V5J 5J8, Canada

HIGHLIGHTS

- A new geometrical model is proposed for catalyst layers.
- An analytical model is derived for thermal conductivity of dry catalyst layers.
- The analytical model is validated by some experimental data.
- Shares of different thermal resistances inside a dry catalyst layer are compared.
- Some design guidelines are provided for optimum catalyst layer designs.

ARTICLE INFO

Article history:
Received 25 November 2016
Received in revised form
20 March 2017
Accepted 21 March 2017
Available online 20 April 2017

Keywords:
Polymer electrolyte membrane fuel cell
Catalyst layer
Thermal conductivity
Transport properties
Overlapping agglomerates
Analytical modeling

ABSTRACT

In this work, a closed form expression is derived to describe thermal conductivity of dry catalyst layers (CLs) used in automotive polymer electrolyte membrane fuel cells (PEMFCs). This expression is based on a new geometrical description of the CL which features: i) overlapping agglomerates, and ii) four main scales of pores: macropores between the agglomerate clusters, mesopores between the agglomerates, micropores between the carbon particles inside the agglomerates, and sub-nanometer pores inside the carbon particles. Under certain simplifying assumptions, this leads to a three-scale unit cell model which can be solved analytically for the effective thermal conductivity. The model predictions agree well with experimental data for a dry CL. Based on the developed model, shares of different resistances inside the CL are calculated for a reference design and compared to one another, and a comprehensive parametric study is performed to assess the effects of different design parameters of the CL. In addition, based on the results of the parametric study, some design guidelines are provided for designing CLs with optimum transport properties.

1. Introduction

Heat generation in a polymer electrolyte membrane fuel cell (PEMFC) occurs due to: 1) reversible (or entropic) heat of the electrochemical reactions in the catalyst layers (CLs), 2) irreversible heat due to losses caused by over-potential in the CLs, 3) latent heat due to phase change in the cathode CL, 4) Joule heating in all of the membrane electrode assembly (MEA) layers including the CLs, and 5) heat of sorption of water vapor inside the ionomer in the CLs [1–4]. The above heat sources could induce significant local temperature variations inside the MEA which could highly affect water management, performance, and degradation of the fuel cell during normal operation as well as special operating conditions like freeze-start, warmup, and others [2–10]. Despite the comparatively low thickness of the CLs within the current state of the art MEAs, Burheim at al [11]. predict a significant change in the MEA temperature profile due to saturation of the CLs alone.

The non-isothermal MEA models cited above rely on explicit prescription of thermal conductivity for the CLs and, therefore, are limited to sensitivity studies on this parameter alone. To enable a model-guided structural and compositional optimization of the MEA, a predictive description of the thermal conductivities with respect to the structural parameters is necessary.

So far, some theoretical and experimental studies have been performed on the thermal conductivities of different MEA components [3,11–32]. However, all the performed studies on the thermal conductivity of the CL [3,11,24,25] are purely experimental, and, to the authors' best knowledge, no expression for the thermal conductivity of the CL can be found in the open literature. Such expressions are necessary to correlate the thermal conductivity of

DOI of original article: http://dx.doi.org/10.1016/j.jpowsour.2017.02.016.
* Corresponding author.
E-mail addresses: mahadi@sfu.ca (M. Ahadi), andreas.putz@afcc-auto.com (A. Putz), juergen.stumper@afcc-auto.com (J. Stumper), mbahrami@sfu.ca (M. Bahrami).

http://dx.doi.org/10.1016/j.jpowsour.2017.03.100
0378-7753/

Nomenclature

A	Cross sectional area (m^2)
a	Contact or overlap radius (m)
c	Specific heat capacity ($J \cdot kg^{-1} \cdot K^{-1}$)
D	Gap profile (m)
d	Differential operator
E	Young's modulus (Pa)
F	External force (N)
k	Thermal conductivity ($W \cdot m^{-1} \cdot K^{-1}$)
L	Characteristic length (m)
l	Loading (mass ratio)
M	Gas parameter (m)
m	Mass (kg)
n	Number of particles
P	Pressure (Pa)
Q	Heat flow rate (W)
R	Thermal resistance ($K \cdot W^{-1}$)
r	Radius (m)
S	Surface area (m^2)
T	Temperature (K)
t	Thickness (m)
V	Volume (m^3)
v	Speed of sound or phonons in the medium ($m \cdot s^{-1}$)
x	x-coordinate of Cartesian coordinate system (m)
y	y-coordinate of Cartesian coordinate system (m)
z	z-coordinate of Cartesian coordinate system (m)

Greek letters

β	A constant parameter
δ	Strain
ε	Porosity
η	A parameter (m), $\eta = r - \omega_z + M/2$
θ	Overlap or contact angle (rad)
Λ_p	Mean free path of phonons (m)
λ	Normalized dimension, $\lambda = L/\Lambda_p$
ν	Poisson's ratio
ρ	Density ($kg \cdot m^{-3}$)
χ	Volume fraction of macropores
ψ	Ionomer coverage
Ω	Adhesion work per unit area ($J \cdot m^{-2}$)
ω	Overlap depth or deformation (m)

Subscripts

I	Related to two overlapping spheres with the side caps
II	Related to the side caps of two overlapping spheres
ac	Agglomerate cluster
agg	Aggregate of Pt/C particles inside an agglomerate
aggl	Agglomerate: a microstructural unit made from aggregate of Pt/C particles and the ionomer film around it
b	Bulk
bot	Bottom
C	Carbon
cl	Catalyst layer
con	Constriction
cs	Cap segment
g	Gas
i	Ionomer
map	Macropore
mep	Mesopore
meu	Mesoscale unit cell
mip	Micropore
miu	Microscale unit cell
noa	Non-overlapping area
oa	Overlapping area
Pt	Platinum
Pt/C	A carbon particle together with the platinum particles supported on it considered as a whole
spr	Spreading
top	Top
x	In-plane direction
z	Through-plane direction

Superscripts

*	Property divided by the reference property
–	Effective property

the CL to its salient structural parameters.

In this work, by adopting a unit cell approach, a detailed closed-form expression is developed for the thermal conductivity of a dry CL, for the first time. An experimental study is performed [33] proposing a new method for deconvoluting contact resistances and other residuals for a residual-free measurement of the bulk thermal conductivity of a CL, and the results of the model are compared to and successfully validated by our experimental data.

2. Microstructure of the CL

Traditional ink-based CLs are complex porous composites of three distinct materials: 1) nano-sized (~2–5 nm) catalyst particles (typically platinum (Pt) or its alloys), 2) nano-sized (~20–30 nm) carbon (C) particles which support the platinum particles, and 3) an ion-conducting polymeric material for which perfluorosulfonic acid (PFSA) ionomers are generally used. High resolution CL images [34] and molecular dynamics simulations of catalyst ink solidification [35] indicate that carbon particles cluster and form aggregate-like structures covered by a thin film of ionomer. In this work, the word “aggregate” is used to refer to the group of Pt/C particles which is covered by the ionomer film, and the word “agglomerate” is used to refer to the Pt/C aggregate and its surrounding ionomer film together. Scanning electron microscope (SEM) images of a CL (fractured in liquid nitrogen) reported by Ref. [34] show that existence of some macropores (~600–1000 nm), between clusters of agglomerates, may be considered as another geometrical characteristic of a CL.

3. Geometrical modeling of the CL

Several approaches to geometrical modeling of the CL have been proposed in literature. Common approaches are: i) pseudo-homogeneous film or macro-homogeneous model (MHM) [36–38], ii) agglomerate model (AM) [39–42], and iii) microstructure reconstruction model (MRM) [43–45]. A brief review of the features of the available models is provided in Table 1.

In this study, a new geometrical model, shown in Fig. 1, is proposed for a CL. This model does not have most of the limitations of the available models in literature, as described in Table 1. Details on the ranges of nanoparticles sizes, carbon black microstructure, ionomer film thickness, and location of platinum particles on carbon black particles, specified in the geometrical model shown in Fig. 1, are gathered from Refs. [46–48].

As shown in Fig. 1, the proposed geometrical model consists of overlapping agglomerates (spherical shape) making clusters

Table 1
Summary of the features of the available geometrical models for the CL in literature.

Model	Features
MHM [36–38]	• Assuming a homogeneous configuration of Pt, C, and ionomer in the porous matrix of the CL (treating the CL as an effective porous medium) • Using prescribed transport properties for the CL, to be determined from experiments or structural models • Lacking microstructural or morphological details of the CL
AM [39–42]	• Assuming structural units of the CL as spherical Pt/C agglomerates filled with ionomer or liquid water • Assuming possible presence of a thin ionomer film around a cluster • Assuming possible presence of a thin liquid water film around a cluster • Existence of analytical solutions for specific cases
MRM [43–45]	• Obtaining a reconstruction of the CL microstructure from micrographs or random algorithms • Solving the transport and reaction equations within the reconstructed microstructure of the CL via direct numerical simulation (DNS) • Necessity of performing numerical simulations with a suitable solver for a system of nonlinearly coupled partial differential equations on multiple domains (high calculation time and cost)

around some macropores. Moreover, this geometrical model considers four types of pores in the CL: i) macropores (a couple of hundreds of nanometers) between the agglomerate clusters, ii) mesopores (a couple of tens of nanometers) between the agglomerates, iii) micropores (a couple of nanometers) between the carbon particles inside the agglomerates, and iv) sub-nanometer pores inside the porous carbon particles. In this study, all the aforementioned four types of pores are addressed. Moreover, the bulk ionomer which may inhomogeneously be distributed in the mesopores is considered as a part of the ionomer film around the agglomerates, and the thickness of the ionomer film is considered to be uniform throughout the ionomer-covered surface of the agglomerates. Geometrical relations for the agglomerates and the Pt/C aggregates inside the agglomerates can be found in Appendix A.

4. Modeling thermal conductivity of the CL

A multi-scale unit cell approach is adopted to derive a closed form

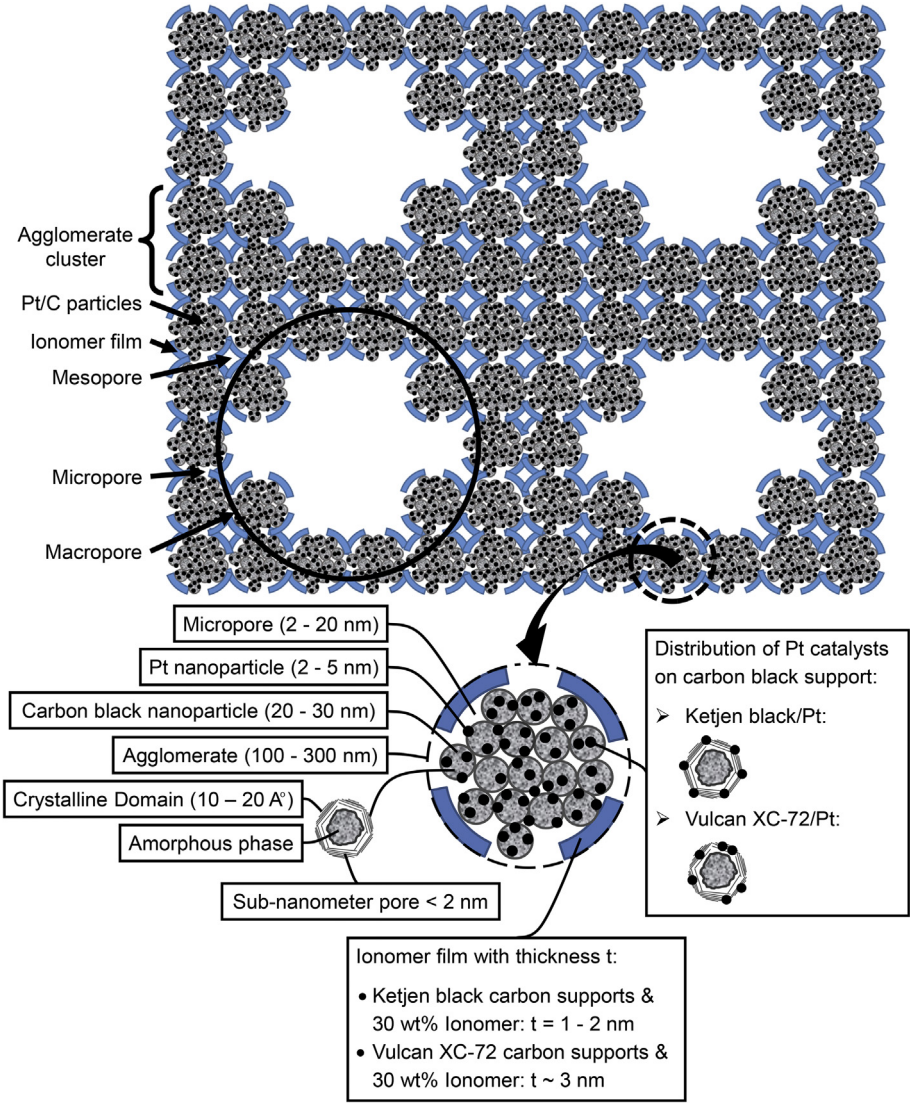

Fig. 1. Proposed geometrical model for the CL.

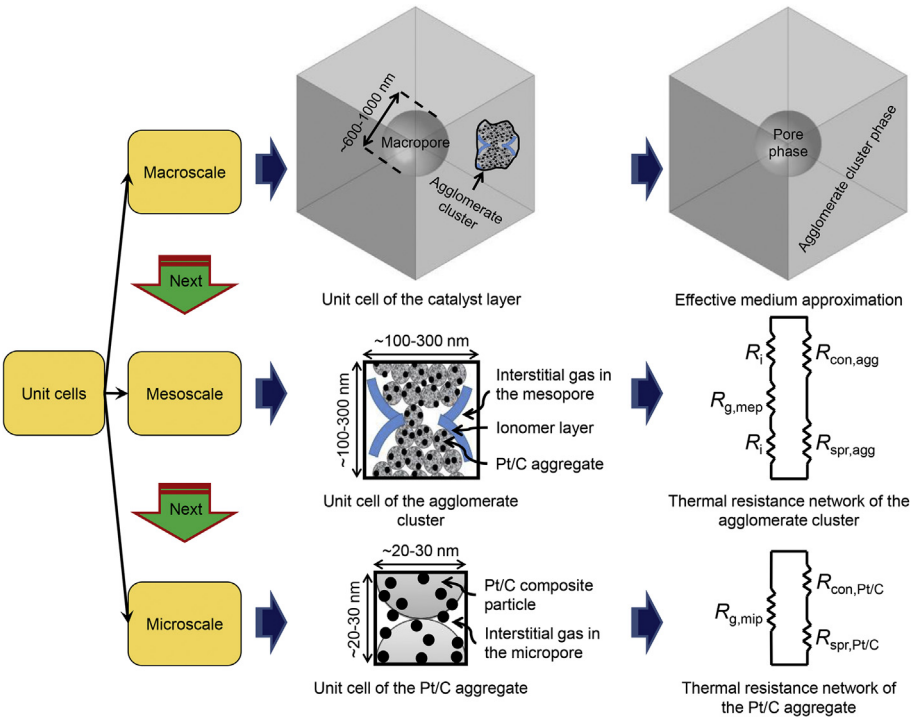

Fig. 2. Proposed multi-scale unit cells model for modeling thermal conductivity of the CL.

expression for the effective thermal conductivity of the CL. The proposed geometrical model, shown in Fig. 1, dictates the chain of unit cells and their relevant thermal resistance networks shown in Fig. 2. As shown in Fig. 2, three scales of unit cells are considered: i) a macroscale unit cell in which agglomerates are clustered around a macropore at the middle of the cell; ii) a mesoscale unit cell which is the unit cell of an agglomerate cluster around the macropore; and iii) a microscale unit cell which represents the unit cell of a Pt/C aggregate inside an agglomerate in the cluster. As shown in Fig. 2, the macropore between the agglomerate clusters (see Fig. 1) is considered as a spherical pore in the middle of the macroscale unit cell. For simplicity, a simple cubic (SC) arrangement is considered for the unit cells of the agglomerate cluster and Pt/C aggregate. In the following subsections, thermal conductivity of the CL at macro-, meso-, and micro-scales is modeled by using the developed unit cells for different scales, and the developed models for different scales are then coupled to yield the effective thermal conductivity of the CL.

4.1. Modeling thermal conductivity of the CL at macroscale

Maxwell [49] derived an analytical model for effective thermal conductivity of a composite material consisting of sparsely distributed spherical particles in another medium. Following the Maxwell's model [49] and assuming that the entire macroscale unit cells, making the CL, can be treated like a composite medium consisting of sparsely distributed macropores in clusters of agglomerates (see Fig. 1 and Fig. 2), the effective thermal conductivity of the CL can be found from:

$$k_{cl} = \frac{3k_{ac}k_{map}\chi + (2k_{ac} + k_{map})k_{ac}(1-\chi)}{3k_{ac}\chi + (2k_{ac} + k_{map})(1-\chi)} \tag{1}$$

where χ is the volume fraction of macropores in the CL and $k_{map} = k_g$ for a dry CL. If we define porosity of the agglomerate clusters around the macropores (ε_{ac}) as the volume fraction of pores in the clusters and porosity of the CL (ε_{cl}) as the volume fraction of all the pores in the CL including the macropores, the following relation holds between χ, ε_{ac}, and ε_{cl}:

$$\chi = 1 - \frac{1-\varepsilon_{cl}}{1-\varepsilon_{ac}} \tag{2}$$

where ε_{ac} is found from the following relation (see Appendix B for the derivation of ε_{ac}):

$$\varepsilon_{ac} = 1 - \pi^2(1-\varepsilon_C)\left[1 + l_{Pt}\frac{\rho_C}{\rho_{Pt}} + \frac{\rho_C l_i(1+l_{Pt})}{\rho_i(1-l_i)}\right] \times \frac{\frac{4}{3} - \left[1-\cos\left(\frac{\theta_{agg}}{2}\right)\right]\left\{3\sin^2\left(\frac{\theta_{agg}}{2}\right) + \left[1-\cos\left(\frac{\theta_{agg}}{2}\right)\right]^2\right\}}{48\cos^3\left(\frac{\theta_{agg}}{2}\right)} \tag{3}$$

where l_{Pt} is the platinum loading, defined as the mass of platinum over the mass of carbon; l_i is the ionomer loading, defined as the mass of ionomer over the total mass of the CL, and θ_{agg} is the overlap angle of the aggregates (see Fig. A1 and Fig. C1 a). Eqs. (2) and (3) show that, for a certain composition of the CL (fixed ε_C, l_{Pt}, and l_i), ε_{cl} is a function of χ and θ_{agg}; therefore, by having two of the ε_{cl}, χ, and θ_{agg}, the third one could be determined from Eqs. (2) and (3). In this work, ε_{cl} and χ were estimated from transmission electron microscope (TEM) images of the CL, and the value of θ_{agg} was determined from Eqs. (2) and (3), accordingly.

4.2. Modeling thermal conductivity of the CL at mesoscale

The unknown effective thermal conductivity of the agglomerate clusters in Eq. (1), i.e. k_{ac}, is obtained from thermal resistance of the mesoscale unit cell as follows:

$$k_{ac} = \frac{t_{meu}}{R_{meu}A_{meu}} \tag{4}$$

where t_{meu} is the thickness of the mesoscale unit cell across which

the heat transfer occurs; R_{meu} is the thermal resistance of the mesoscale unit cell, and A_{meu} is the cross-sectional area of the mesoscale unit cell through which the heat transfers. t_{meu} and A_{meu} are simply obtained from the geometry of the mesoscale unit cell as follows (see Fig. A1):

$$t_{meu} = 2\left(r_{agg} - \omega_{agg}\right) \tag{5}$$

$$A_{meu} = t_{meu}^2 \tag{6}$$

where ω_{agg} is the overlap depth of the aggregates (see Fig. A1 and Fig. C1 a). R_{meu} in Eq. (4) is calculated based on the relevant thermal resistance network shown in Fig. 2, as follows:

$$R_{meu} = \left[\frac{1}{R_{g,mep} + 2R_i} + \frac{1}{R_{con,agg} + R_{spr,agg}}\right]^{-1} \tag{7}$$

Thermal resistance of the interstitial gas in the mesopore, i.e. $R_{g,mep}$, is modeled by adopting the same approach taken by Bahrami et al. [50] for modeling the thermal resistance of a gas filling the space between two non-overlapping spheres. In this study, first, we derive a general model for gas resistance between two overlapping spheres with equal radii, and then we use the developed model to obtain the gas resistances in the mesopore and the micropore (see Appendix C for the derivation details). Considering a general geometry for conduction through the gas between two overlapping spheres with equal radii in a packed bed of spheres having an SC arrangement, as shown in Fig. C1 a, the general model for the gas resistance is obtained as:

$$R_g = \frac{1}{k_g}\left[\pi r \ln\left(\frac{\eta}{\eta - r\cos(\theta_x/2)}\right) - 2\pi r \times \left\{\frac{2\eta}{\sqrt{\eta^2 - r^2}}\left[\tan^{-1}\left(\frac{r}{\sqrt{\eta^2 - r^2}}\right) - \tan^{-1}\left(\frac{r - \eta\tan(\theta_z/4)}{\sqrt{\eta^2 - r^2}}\right)\right] - \frac{\theta_z}{2}\right\}\right]^{-1} \tag{8}$$

where $\eta = r - \omega_z + M/2$. In this study, we assume that all the agglomerates have the same radius of r_{aggl}; moreover, we assume that $\theta_{aggl,x} = \theta_{aggl,z} = \theta_{aggl}$, $a_{aggl,x} = a_{aggl,z} = a_{aggl}$, and $\omega_{aggl,x} = \omega_{aggl,z} = \omega_{aggl}$ (see Fig. C1 a for a pictorial definition of the terms).

Since, the ionomer thickness is relatively low in comparison with the surface of the aggregate which it covers, the ionomer film around the aggregate can be regarded as a thin spherical shell, and therefore, thermal resistance of the ionomer in Eq. (7) can simply be obtained from the slab formula, as follows:

$$R_i = \frac{t_i}{k_i A_i} \tag{9}$$

where A_i is the surface of ionomer on half of the aggregate, obtained from:

$$A_i = \psi\left\{2\pi r_{agg}^2 - 3\pi\left(a_{agg}^2 + \omega_{agg}^2\right)\right\} \tag{10}$$

where ψ is ionomer coverage on the surface of the aggregate, which is defined as the fraction of the available surface of the aggregate (excluding the overlapping parts) covered by the ionomer, and $\{2\pi r_{agg}^2 - 3\pi(a_{agg}^2 + \omega_{agg}^2)\}$ is the available surface of half of the aggregate. As shown in Appendix D, the relation for the ionomer thickness, t_i in Eq. (9), is derived as:

$$t_i = \frac{4\pi\rho_C n_C r_C^3 l_i (1 + l_{Pt})(1 - \varepsilon_C)}{3\rho_i (2A_i)(1 - l_i)} \tag{11}$$

where n_C is the number of carbon particles in the aggregate which is obtained from (see Appendix D for the derivation):

$$n_C = \frac{\frac{4}{3}\pi r_{agg}^3 - \frac{\pi}{6}\omega_{agg}\left(3a_{agg}^2 + \omega_{agg}^2\right) \times 6}{(2r_C)^3} \tag{12}$$

The next step is to model constriction and spreading resistances of the aggregate of Pt/C particles, i.e. $R_{con,agg}$ and $R_{spr,agg}$ in Eq. (7). Since the aggregate is made of microscale unit cells (see Fig. 2), one approach for modeling such a complex geometry is to obtain an effective thermal conductivity for a microscale unit cell and assume that the aggregate is consisted of series rows of parallel microscale unit cells, as shown in Fig. 3. Such an assumption leads to parallel isotherms in each section of the aggregate, with isotherms being parallel to the rows of microscale unit cells; consequently, as shown in Appendix E, considering a differential slab element between two infinitely close isotherms (see Fig. 3), spreading or constriction resistance of the aggregate can be found by integration as follows:

$$R_{con,agg} = R_{spr,agg} = R_{agg,noa} + R_{agg,oa} \tag{13}$$

where $R_{agg,noa}$ and $R_{agg,oa}$ are the resistances of half of the aggregate

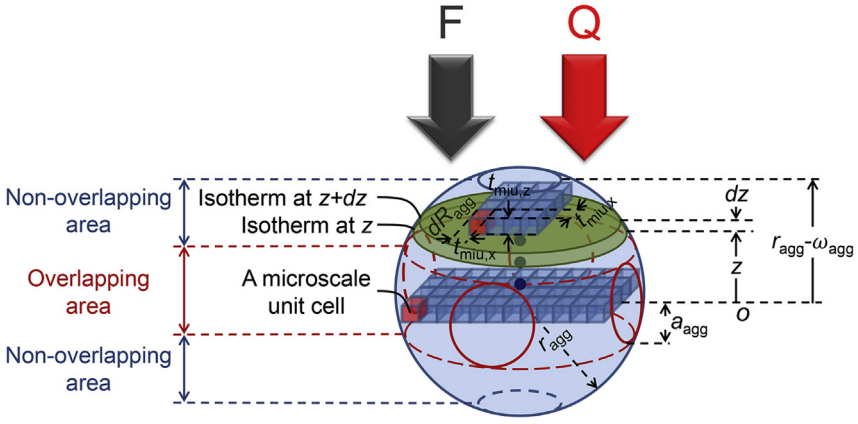

Fig. 3. Integrating inside the aggregate to obtain its spreading or constriction resistance.

inside the non-overlapping area and the overlapping area, respectively, and are obtained from:

$$R_{agg,noa} = \frac{1}{2\pi k_{agg} r_{agg}} \ln\left(\frac{(2r_{agg} - \omega_{agg})(r_{agg} - a_{agg})}{\omega_{agg}(r_{agg} + a_{agg})}\right) \quad (14)$$

$$R_{agg,oa} = \frac{1}{k_{agg}} \times \int_0^{a_{agg}} \frac{dz}{\left(\begin{array}{c} -\pi\left(r_{agg}^2 - z^2\right) + 4(r_{agg} - \omega_{agg})\sqrt{r_{agg}^2 - (r_{agg} - \omega_{agg})^2 - z^2} \\ +4\left(r_{agg}^2 - z^2\right)\tan^{-1}\left(\frac{r_{agg} - \omega_{agg}}{\sqrt{r_{agg}^2 - (r_{agg} - \omega_{agg})^2 - z^2}}\right) \end{array}\right)} \quad (15)$$

4.3. Modeling thermal conductivity of the CL at microscale

The unknown effective thermal conductivity of the Pt/C aggregate, i.e. k_{agg} in Eqs. (14) and (15), is obtained from thermal resistance of the microscale unit cell shown in Fig. 2, as follows:

$$k_{agg} = \frac{t_{miu,z}}{R_{miu} A_{miu}} \quad (16)$$

where $t_{miu,z}$ is the thickness of a microscale unit cell across which the heat transfer occurs (see Fig. 3), R_{miu} is the thermal resistance of the microscale unit cell, and A_{miu} is the cross sectional area of the microscale unit cell through which the heat transfers. A_{miu} is obtained from the geometry of the microscale unit cell as follows:

$$A_{miu} = t_{miu,x}^2 \quad (17)$$

Relations for $t_{miu,x}$ and $t_{miu,z}$ are derived further in this section. Efforts were made to simplify the complex microstructure of the microscale unit cell for analytical modeling of its thermal resistance, R_{miu}, by regarding each carbon particle and the platinum particles supported on it as one composite particle. Accordingly, effective properties like thermal conductivity, Young's modulus, and Poisson's ratio were sought for a composite Pt/C particle inside the microscale unit cell by using the bounds and models provided for these properties in Ref. [51]. However, less than 1% change in the effective properties versus the platinum loading was predicted in the practical range of platinum loading of the CL, meaning that a composite Pt/C particle inside the microscale unit cell can simply be regarded as a carbon particle for the purpose of thermal and mechanical modeling. Considering this simplification, the equivalent thermal resistance network of the microscale unit cell, shown in Fig. 2, yields the following relation for R_{miu}:

$$R_{miu} = \left[\frac{1}{R_{g,mip}} + \frac{1}{R_{con,Pt/C} + R_{spr,Pt/C}}\right]^{-1} = \left[\frac{1}{R_{g,mip}} + \frac{1}{R_{con,C} + R_{spr,C}}\right]^{-1} \quad (18)$$

Since carbon nanoparticles have a high surface area to volume ratio (~10^8 m^2/m^3), the effect of surface forces between them cannot be neglected. The surface forces between two adjacent carbon particles result in an initial contact between them which can further be increased by imposing an external force, like a clamping force, on the particles. Hertzian theory [52] models the deformation of two contacting elastic spheres in the presence of an external force, but it doesn't take the effects of surface forces between the spheres into account, which results in a zero contact area in the absence of any external force. However, in the case of nanoparticles, surface forces between the nanoparticles are considerable and play a major role in their contact and deformation behavior [53], even in the absence of any external force. So far, many theories have been proposed for extending the Hertzian theory by accounting for surface forces between the contacting nanoparticles [53–56]. In this study, assuming that carbon particles can be regarded as elastic spheres, the contact between two contacting carbon particles is modeled by the Derjaguin–Muller–Toporov (DMT) model [55], which describes contact mechanics between very small and hard bodies with low surface energies. According to the DMT model [55], for particles with the same radius, r, which are under an external force, F, the contact radius, a (see Fig. C.1 a), is determined from:

$$a = \left[\frac{3\bar{r}}{4\bar{E}}(F + 2\pi\bar{r}\Omega)\right]^{1/3} \quad (19)$$

where $\bar{r} = r/2$, $\bar{E} = E/[2(1-\nu^2)]$, and Ω is the adhesion work per unit area for the particles. It is worthy to mention that the term $2\pi\bar{r}\Omega$ in Eq. (19) is, in fact, the adhesion force between two particles which is added to the external force, F, to obtain the total force between the particles; by neglecting the term $2\pi\bar{r}\Omega$, Eq. (19) will turn into the Hertzian model [52]. Before using Eq. (19) for the carbon particles in the CL, it should be noted that the carbon particles experience an external clamping force in the through-plane direction of the CL and no external force in the in-plane direction, due to limitation of movement of the CL and other layers of the MEA only in the through-plane direction (direction of the clamping force) and their free movement in the in-plane direction. Therefore, according to Eq. (19), the carbon particles will have different contact radii in the through-plane and in-plane directions (see Fig. C1 a) which are obtained from:

$$a_{C,z} = \left[\frac{3\pi\bar{r}_C^2\Omega_C}{2\bar{E}_C}\right]^{1/3} \quad (20)$$

$$a_{C,x} = \left[\frac{3\bar{r}_C}{4\bar{E}_C}\left(F_C + 2\pi\bar{r}_C\Omega_C\right)\right]^{1/3} \quad (21)$$

where F_C is obtained from (see Eq. (17) for the substitution of A_{miu}):

$$F_C = \frac{P_{cl} A_{miu}}{1-\varepsilon_{cl}} = \frac{P_{cl} t_{miu,x}^2}{1-\varepsilon_{cl}} \tag{22}$$

where $t_{miu,x}$ is obtained from:

$$t_{miu,x} = 2(r_C - \omega_{C,x}) \tag{23}$$

where the deformation of the carbon particles in the in-plane direction, i.e. $\omega_{C,x}$ (see Fig. C.1 a), is found by using $a_{C,z}$ from Eq. (20) as follows:

$$\omega_{C,x} = r_C - \sqrt{r_C^2 - a_{C,z}^2} \tag{24}$$

Having found the contact radii of the carbon particles, i.e. $a_{C,z}$ and $a_{C,x}$ from Eqs. (20) and (21), the deformation of the particles in the through-plane direction, i.e. $\omega_{C,z}$ (see Fig. C1 a), and the contact angles of the particles, i.e. $\theta_{C,x}$ and $\theta_{C,z}$ (see Fig. C1 a), are calculated from:

$$\omega_{C,z} = r_C - \sqrt{r_C^2 - a_{C,x}^2} \tag{25}$$

$$\theta_{C,x} = 2\sin^{-1}\left(\frac{a_{C,x}}{r_C}\right) \tag{26}$$

$$\theta_{C,z} = 2\sin^{-1}\left(\frac{a_{C,z}}{r_C}\right) \tag{27}$$

Using $\omega_{C,z}$ from Eq. (25), $t_{miu,z}$ is obtained from:

$$t_{miu,z} = 2(r_C - \omega_{C,z}) \tag{28}$$

The strain of a carbon particle in this model can simply be obtained from the strain of the microscale unit cell. Knowing that uncompressed and compressed thicknesses of the microscale unit cell under the external force are $t_{miu,x}$ and $t_{miu,z}$, respectively, the following relation can be used to calculate the strain of a carbon particle:

$$\delta_C = \frac{t_{miu,x} - t_{miu,z}}{t_{miu,x}} \tag{29}$$

The resistance $R_{g,mip}$ in Eq. (18) can then be calculated by using Eq. (8) for the carbon particles. Moreover, $R_{con,C}$ and $R_{spr,C}$ in Eq. (18) are obtained from the half-space model [57]:

$$R_{con,C} = R_{spr,C} = 1 \Big/ \left(4\overline{k_C} a_{C,x}\right) \tag{30}$$

where $\overline{k_C}$ is the effective thermal conductivity of a porous carbon particle. While using the half space model (Eq. (30)) to obtain the spreading/constriction resistance in a carbon particle, the behavior of the heat flow lines in the immediate vicinity of the contact area between the contacting particles is of interest. According to the multifaceted geometry of a carbon particle shown in Fig. 1, in the vicinity of the contact area, during spreading/constriction of the heat flow lines, the entering/exiting heat has to pass a parallel configuration of layers of graphitic carbon and gas-filled gaps inside the particle. Considering the much higher conductivity in the in-plane direction of graphite compared to its through-plane direction, the heat flow lines should bend toward the in-plane direction of graphitic layers in the vicinity of the contact area and should mostly be affected by the graphitic layers rather than the gas (air) inside the gaps. Moreover, far from the contact area and toward the middle region of a particle, the heat flow lines should spread more or less along the in-plane direction of the graphitic layers covering the particle. Therefore, the effective thermal conductivity of a porous carbon particle for use in Eq. (30) seems to be appropriately approximated by the parallel model [51], as follows:

$$\overline{k_C} = (1-\varepsilon_C)k_C + \varepsilon_C k_g \tag{31}$$

Up to this point, all the derived equations can be used for both macroscopic and microscopic systems, except for Eqs. (9) and (30) which are derived based on the macroscopic Fourier's law of heat conduction and need to be corrected for use in the nanoscale ionomer film and carbon particle. Such a correction can simply be made by correcting the thermal conductivity values of ionomer in Eq. (9) and carbon in Eq. (31), to account for nanoscale effects, like phonon mean free path and size-dependent effects, on the conduction heat transfer in nanoscale. Ordonez-Miranda et al. [58] solved the Boltzmann transport equation, analytically, for steady state heat transfer inside a thin film and proposed a modified thermal conductivity which could be used in the Fourier's law of heat conduction to predict the heat transfer in the film. This modified thermal conductivity is proposed in Ref. [58] as:

$$k = \frac{k_b}{1 + 2\beta/\lambda} \tag{32}$$

where $\beta \approx 2/3$, $\lambda = L/\Lambda_p$ is the layer thickness normalized by the mean free path of phonons inside the material, and $k_b = \rho c v \Lambda_p/3$ is the bulk or macroscopic thermal conductivity of the material. In this work, modified thermal conductivity values found from Eq. (32) are used in Eqs. (9) and (31) to account for size-dependent effects. For this purpose, L is chosen as the carbon particle diameter for finding k_C and the ionomer film thickness for finding k_i, and the mean free path of phonons inside each of the materials is calculated from:

$$\Lambda_p = \frac{3k_b}{\rho c v} \tag{33}$$

4.4. Multi-scale coupling

The developed thermal conductivity models for different scales are coupled to yield the thermal conductivity of the CL. For this purpose, the value of k_{agg} found from the microscale model (section 4.3) is used in the mesoscale model (section 4.2) to find k_{ac}, and then the found value for k_{ac} is used in the macroscale model (section 4.1) to find k_{cl}.

To validate the present model, in a separate study [33], CL samples were coated on aluminum (Al) and ethylene tetrafluoroethylene (ETFE) substrates and measured under different compressive loads by a guarded heat flow (GHF) testbed, as per ASTM E1530-11 standard, as well as a transient plane source (TPS), as per a modified TPS method for thin films proposed in Ref. [59]. The microstructural properties of the CL of Ref. [33], used for validating the model, are shown in Table 2.

Among the values shown in Table 2, l_{Pt} and l_i were directly determined from the catalyst ink composition; the values of ε_{cl}, r_C, r_{agg}, and χ were estimated from TEM images taken from the CLs, and the value of ε_C was found from literature [60]. Moreover, the value of ψ was roughly chosen based on the available ranges in literature [61]. However, as shown later in section 5 of this article, thermal conductivity of the CL is highly insensitive to the value of ψ (and r_{agg} as well); therefore, any value could be chosen for ψ (as well as for r_{agg}) without introducing much error into the thermal conductivity results from the model. In addition, for validating the model, thermophysical properties of dry air were used for the gas

Table 2
Microstructural properties of the CL of Ref. [33] (reference design).

Parameter	Value
l_{Pt}	1.1
l_i	0.34
ϵ_{cl}	0.7
r_C	10 (nm)
r_{agg}	50 (nm)
χ	0.46
ϵ_C	0.287 [60]
ψ	0.5 [61]

filling the pores, and thermophysical properties of graphite and Nafion were used for the bulk of carbon particles and ionomer, respectively.

5. Results and discussion

5.1. Model validation

Thermal conductivity results of the model are plotted next to the experimental thermal conductivity data of Ref. [33] in Fig. 4. As shown in Fig. 4, the modeling results agree well with the experimental data.

The analytical results of Fig. 4 show that there should be some slight increase (~14%) in the thermal conductivity of the CL with increasing pressure from 2 to 15 bar, which is originated from the resultant increase in the size of contact points between the carbon particles (see Eqs. (21) and (22)). However, as shown in Fig. 4, this small increase falls in the uncertainty ranges of the experimental data and, therefore, cannot be captured experimentally. The model predictions for strain of a carbon particle, calculated from Eq. (29), also show a very slight compressibility for a carbon particle (~0.2% at 15 bar) which justifies the observed small increase in the thermal conductivity with increasing pressure. It is worthy to mention that thickness measurements for catalyst-coated substrates in the 0–30 bar pressure range also indicated that CL is highly incompressible in this pressure range [33].

5.2. Shares of different resistances inside the CL

Shares of different resistances inside the CL are predicted by the model for the CL of Ref. [33] (see Table 2) at 2 bar pressure and shown in Table 3. As shown in Table 3, gas resistance has the largest share in both the microscale and the mesoscale. Also, in the mesoscale, resistance of the ionomer is comparable with the resistance of the aggregate, but the series configuration of the ionomer resistance and the resistance of the gas in the mesopore makes a highly resistant pathway for heat and leads most of the passing heat to the much smaller parallel resistance of the aggregate. Overall, the carbon particles and the aggregates of carbon particles make the dominant pathways for heat conduction inside the CL in micro- and meso-scales, respectively.

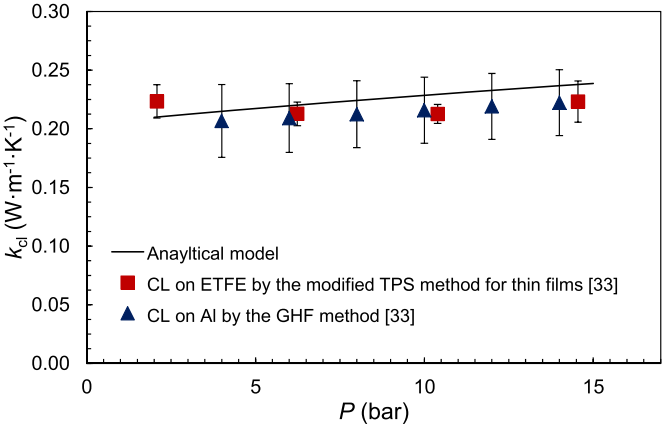

Fig. 4. Thermal conductivity of the CL versus pressure.

Table 3
Shares of different resistances inside the CL at 2 bar pressure.

Different scales	Microscale			Mesoscale			
Resistances	$R_{g,mip}$	$R_{con/spr,C}$	R_{miu}	$R_{g,mep}$	R_i	$R_{con/spr,agg}$	R_{meu}
Magnitudes (GK W^{-1})	19.566	0.029	0.058	1.812	0.014	0.012	0.025

5.3. Parametric study

In this section, a comprehensive parametric study is performed to investigate sensitivity of the model to changes in different key parameters of the CL. To facilitate analysis of the numerical results, when compositional or structural parameters are changed, the measured CL design (see Table 2) at 2 bar pressure is selected as a reference, and the results are reported relative to this reference. Moreover, when a parameter is studied, the rest of the parameters are kept constant.

5.3.1. Bulk thermal conductivity of carbon, ionomer, and gas (air)

Modeling results show ~8% change in thermal conductivity of the CL when the value of bulk (or macroscopic) thermal conductivity of carbon is changed from 100 to 400 W m^{-1} K^{-1}. This low sensitivity of the model to bulk conductivity of carbon is originated from domination of the size-dependent effects for conduction through a carbon particle; in fact, according to Eqs. (32) and (33), the nature of heat conduction inside a carbon particle is a quasi-ballistic regime dominated by ballistic transport instead of diffusion (refer to Ref. [58] for more details on these regimes). One could easily examine this claim by using the thermophysical properties of bulk graphite in Eq. (33) to find the mean free path of phonons in graphite, substituting the calculated mean free path and the diameter of a carbon particle into Eq. (32), and then playing with the value of bulk conductivity of graphite. By doing so, a value of 126–502 nm is obtained for mean free path of phonons in graphite (for $k_{b,c}$ in the range of 100–400 W m^{-1} K^{-1}) which is way higher than the size of a carbon particle and makes the ballistic transport to be the dominant regime in conduction of heat through a carbon particle. Mathematically speaking, the much higher value of phonon mean free path than the particle diameter results in negligibility of the first term in the denominator of Eq. (32) (i.e. the value 1) compared to the second term of the denominator (i.e. $2\beta_C/\lambda_C$) which contains the size-dependent effects; in limit, only the second term (i.e. $2\beta_C/\lambda_C$) remains in the denominator, and $k_{b,C}$ is cancelled out from the numerator and the denominator of Eq. (32), leaving the size and other thermophysical properties of the particle as the dominant parameters determining the effective conductivity of the particle ($k_C \approx (\rho c v L)_C/4$).

Results also show ~0.04% change in thermal conductivity of the CL when the value of bulk (or macroscopic) thermal conductivity of ionomer is changed from 0.1 to 1 W m^{-1} K^{-1}. However, unlike the case of carbon particles, the reason for this very low sensitivity is that the resistance of the ionomer is masked by the high resistance of the gas in the mesopore which is in a series configuration with the ionomer (see section 5.2). In fact, the model predicts a thickness of ~19 nm and a phonon mean free path of 0.08–0.8 nm for ionomer (for $k_{b,i}$ in the range of 0.1–1 W m^{-1} K^{-1}) which is way lower than the ionomer thickness, leading to the domination of diffusive

transport over the ballistic transport inside the ionomer film.

Results show ~4% change in thermal conductivity of the CL when the value of bulk thermal conductivity of the gas (air) is changed from 0.02 to 0.03 W m^{-1} K^{-1}, pertaining to temperatures of −50 and 80 °C (at atmospheric pressure), respectively. The reason for this low sensitivity is the negligibility of conduction through the gas compared to conduction through the carbon particles (see section 5.2).

5.3.2. Ionomer coverage

The ionomer resistance decreases as the ionomer coverage increases because of the resultant wider spread of the same amount of ionomer on the outer surface of the aggregate, which results in both a higher heat transfer area for the ionomer (see Eq. (10)) and a shorter heat transfer pathway through the ionomer (see Eq. (11)). However, results show that thermal conductivity of the CL is highly insensitive to the ionomer coverage. The reason for this insensitivity is the placement of the ionomer resistance in a series configuration with respect to the high resistance of the gas in the mesopore (see section 5.2).

5.3.3. Radius of Pt/C aggregates

Results show that similar to the case of ionomer coverage, thermal conductivity of the CL is highly insensitive to the radius of aggregates, in the radius range of 50–150 nm (see Fig. 1 for the specified size range). The reason for this behavior could be explained by the interplay between the resultant changes in the values of resistance per unit area (also commonly called insulance) of the agglomerates (i.e. $R_{meu}A_{meu}$) and the length of the heat transfer pathway inside the agglomerates (i.e. t_{meu}). As the modeling results show, increasing the aggregate radius results in more material (or resistance) per unit area of the agglomerate by almost the same factor as lengthening the heat transfer pathway inside the agglomerate. This scaling of the agglomerate insulance and the heat transfer length by more or less the same factor finally leads to a very negligible change in k_{ac} (see Eq. (4)) and, consequently, a very negligible change in k_{cl}.

5.3.4. Radius of carbon particles

As shown in Fig. 5, similar to the case of radius of aggregates, increasing radius of carbon particles results in more microscale insulance ($R_{miu}A_{miu}$) as well as a longer microscale heat transfer pathway ($t_{miu,z}$). However, in this case, the factor of increase in the microscale heat transfer length is higher than the one of increase in the microscale insulance, simply due to the resultant size-dependent increases in contact area between the carbon particles

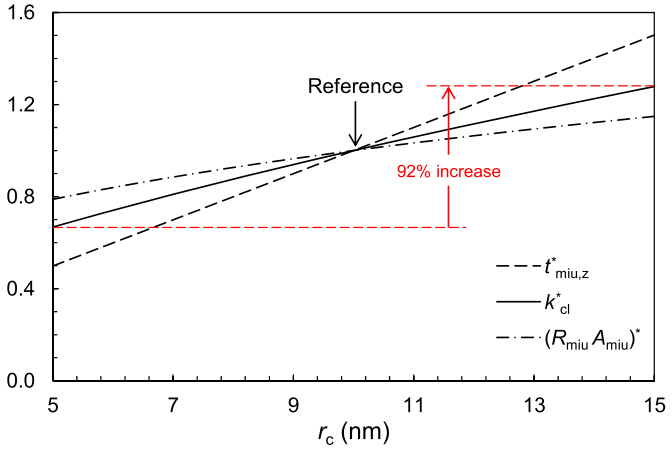

Fig. 5. Parametric study results for radius of carbon particles.

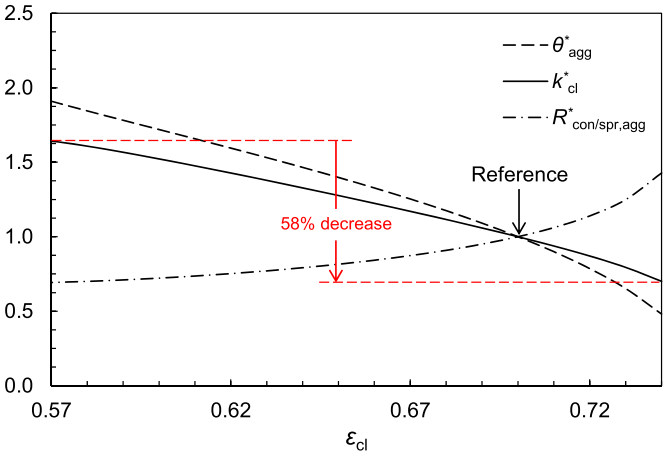

Fig. 6. Parametric study results for CL porosity.

(see Eq. (21)) as well as k_C (see section 5.3.1), counteracting the increase in the microscale insulance. The overall result is a higher microscale thermal conductivity (see Eq. (16)) and, consequently, a higher CL thermal conductivity. It is worth mentioning that enhancing thermal conductivity of the CL by increasing the average radius of carbon particles may also reduce the mass transport resistance inside the agglomerates by increasing the micropore sizes; it may also reduce the electronic resistance inside the CL by increasing the contact area between the carbon particles.

5.3.5. CL porosity

As shown in Fig. 6, by increasing the CL porosity (at a constant volume fraction of macropores), the overlap angle between the aggregates should decrease to make a less compact and more porous agglomerate structure and justify the increase in the CL porosity. This reduction in the overlap between the aggregates leads to narrowing the heat conduction pathway between the aggregates and more spreading/constriction of the heat flow lines at the entrance/exit of the aggregates or, in other words, more spreading/constriction resistance and less conductivity of the aggregates. Consequently, due to the key role of the heat conduction pathway through the aggregates (see section 5.2), thermal conductivity of the CL decreases if its porosity increases by only reducing the overlap (or compactness) of the aggregates or, in other words, if the CL porosity increases by only increasing the volume fraction of small (micro- and meso-) pores inside the CL. This finding is crucial for designing CLs with optimum mass diffusivity and electronic conductivity as well because, generally, smaller pores are also associated with higher mass transport resistance, and because smaller overlap between the aggregates could also increase the electronic resistance of the aggregates.

5.3.6. Volume fraction of macropores

As shown in Fig. 7, by increasing the volume fraction of macropores (at a constant CL porosity), the overlap angle between the aggregates should increase to make a more compact and less porous agglomerate structure and maintain the constant porosity of the CL. This increase in the overlap angle results in reduction in the spreading/constriction resistance of the aggregates, which leads to enhancement in the thermal conductivity of the CL because of the key role of conduction through the aggregates (see section 5.2). Therefore, thermal conductivity of the CL could actually increase by increasing the volume fraction of the macropores if the overlap (or compactness) of the aggregates could be increased in such a way that maintains a constant CL porosity. In fact, in this way, despite replacing the conductive solid parts of the CL by the

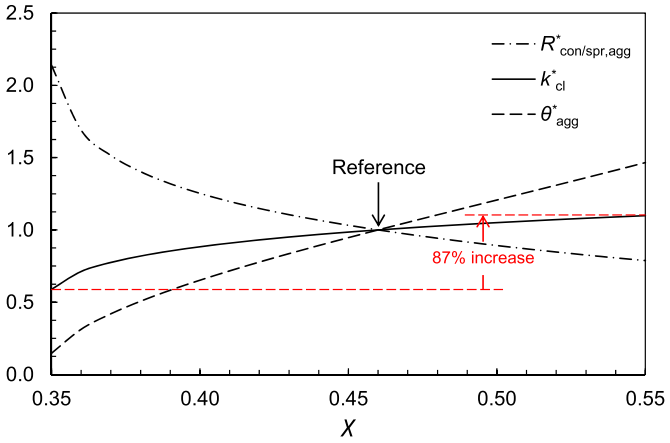

Fig. 7. Parametric study results for volume fraction of macropores.

much less conductive macropores, thermal conductivity of the rest of the solid parts of the CL could be improved to have an overall enhancement in the thermal conductivity of the CL. This finding is of vital importance for CL designers to enhance the mass diffusivity of the CLs without sacrificing their thermal/electrical conductivity or, even better, with enhancing their thermal/electrical conductivity at the same time.

5.3.7. Platinum loading

As shown in Fig. 8, thermal conductivity of the CL decreases by increasing its platinum loading. At this point, it is worth mentioning that although the effects of platinum particles are negligible in thermal resistance at microscale (see the discussion preceding Eq. (18) in section 4.3), they still contribute to the geometry and porosity of the CL (see Eqs. (2) and (3)). As shown in Fig. 8, by increasing the platinum loading (at constant CL porosity and volume fraction of macropores), the overlap (or compactness) of the aggregates should decrease to maintain the constant porosity of the CL, which leads to increase in the spreading/constriction resistance of the aggregates and, consequently, reduction in the thermal conductivity of the CL.

It is worthy to mention here that the observed reduction in the thermal conductivity with increase in the platinum loading is a direct result of keeping other parameters, like the porosity of the CL and volume fraction of macropores, constant. However, in real world, depending on the method of fabrication of the CL, correlations may exist between the porosity of the CL and its platinum loading and/or between the volume fraction of macropores and the

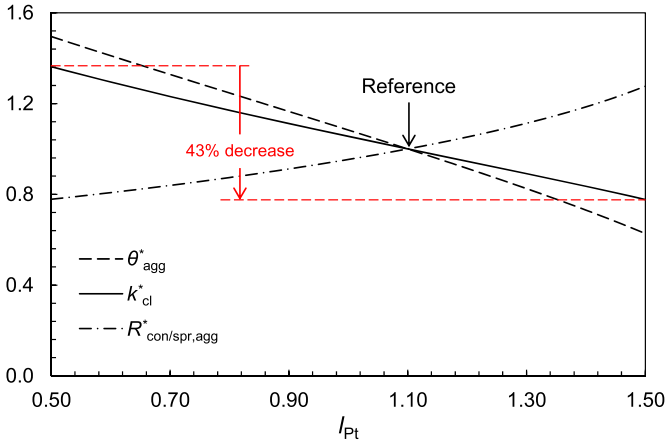

Fig. 8. Parametric study results for platinum loading (defined as the mass of Pt over the mass of C).

platinum loading. In case of existence of such correlations, the porosity of the CL and/or the volume fraction of macropores won't be independent from the platinum loading, and such correlations should also be fed into the model to have a sound prediction of the thermal conductivity by the model. For the purpose of this study, the authors limit their discussion on the effects of platinum loading to the performed standard parametric study.

5.3.8. Ionomer loading

Similar to the case of platinum loading, increasing the ionomer loading (at constant CL porosity and volume fraction of macropores) leads to reduction in the overlap between the aggregates, and consequently, increase in the spreading/constriction resistance of the aggregates; the trends are similar to what shown in Fig. 8. On the other hand, it also results in reduction in the ionomer resistance because of the higher surface area of the ionomer on the aggregates resulted from a lower overlap angle between the aggregates; this effect dominates the effect of the higher thickness of the ionomer on the aggregates resulted from the higher ionomer content. However, since heat conduction through the aggregates is dominant (see section 5.2), the overall effect is reduction in the thermal conductivity of the CL. Similar to the case of section 5.3.7, the results of this section are obtained through a standard parametric study through which all the other parameters are kept constant, and, in case of changing the porosity of the CL and/or volume fraction of macropores with the ionomer loading, such information should also be fed into the model for a sound prediction of thermal conductivity by the model.

6. Conclusions

In this study, a detailed analytical model was developed, for the first time, for thermal conductivity of dry CLs by adopting a multi-scale unit cell approach. The unit cells were chosen based on different microscopic length scales of the CLs such that the developed chain of unit cells could be representative of a CL. The proposed analytical model was validated successfully by experimental data for a dry CL. After model validation, shares of different resistances inside the CL and effects of different parameters were assessed. Results showed that due to very small compressibility of the CL, its thermal conductivity did not change much with compression. The shares of different resistances showed that carbon particles made the dominant pathway for conduction of heat inside the CL. The model showed very low sensitivity to the values of bulk thermal conductivity of carbon, ionomer, and gas (air). It was shown that the nature of heat conduction through the carbon particles is mostly ballistic and highly size-dependent, whereas conduction through the ionomer is dominated by diffusion. Also, the model turned out to be fairly insensitive to the ionomer coverage and radius of Pt/C aggregates, whereas it showed high sensitivity to the radius of carbon particles (size-dependent effects), porosity of the CL, volume fraction of macropores inside the CL, platinum loading, and ionomer loading. It was found that increasing the radius of carbon particles could enhance the thermal conductivity of the CL, whereas increasing the porosity of the CL, platinum loading, and ionomer loading could degrade the thermal conductivity of the CL. It was speculated that increasing the average size of carbon particles may also enhance the mass diffusivity inside the agglomerates and electron transport inside the CL. More importantly, thermal/electrical conductivity of the CL could be enhanced by increasing the volume fraction of the macropores (at a constant CL porosity), which may also be less resistant to mass diffusion inside the CL compared to smaller (micro- and meso-) pores. The geometrical platform presented in this work could be used further to model and

understand other transport properties, like mass diffusivity, electron transport, and proton transport inside the CL. Inclusion of other effects, like humidity and water effects, in the current model is also of great interest and may actually change the shares of the different resistances inside the CL; especially, addition of interconnected macropores is of great interest for modeling humidified or hydrated CLs.

Acknowledgements

The authors gratefully acknowledge the financial support received from the Natural Sciences and Engineering Research Council of Canada (NSERC) through NSERC Collaborative Research Development Grant no. 31-614105. The authors would also like to thank Ms. Jasna Jankovic from Automotive Fuel Cell Cooperation Corp. (AFCC) for assisting in taking and analyzing TEM images of the catalyst layers.

Appendix A. geometrical relations for the agglomerates and Pt/C aggregates inside the agglomerates

The following relations hold for the geometrical parameters of the agglomerates and Pt/C aggregates (see Fig. A.1):

$$a_{agg} = r_{agg}\sin(\theta_{agg}/2) \tag{A.1}$$

$$\omega_{agg} = r_{agg}(1-\cos(\theta_{agg}/2)) \tag{A.2}$$

$$r_{aggl} = r_{agg} + \psi t_i \tag{A.3}$$

$$\omega_{aggl} = \omega_{agg} + \psi t_i \tag{A.4}$$

$$a_{aggl} = \sqrt{r_{aggl}^2 - \left(r_{aggl} - \omega_{aggl}\right)^2} \tag{A.5}$$

$$\theta_{aggl} = 2\sin^{-1}\left(a_{aggl}/r_{aggl}\right) \tag{A.6}$$

It should be noted that because the surface of an aggregate may not be fully covered by the ionomer, ψ is used in Eqs. (A.3) and (A.4) to scale t_i and find the effective values of r_{aggl} and ω_{aggl}, as if $\psi = 1$ and the surface of the aggregate is fully covered by the ionomer (see Eqs. (10) and (11)).

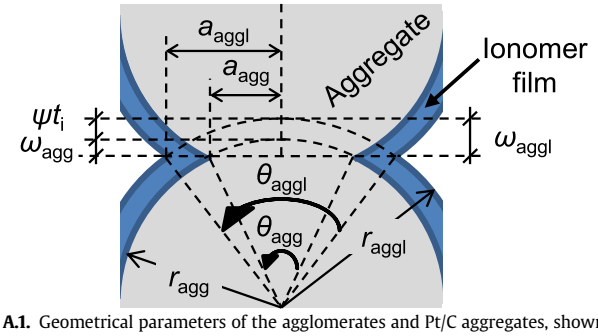

Fig. A.1. Geometrical parameters of the agglomerates and Pt/C aggregates, shown in a mesoscale unit cell.

Appendix B. derivation of the relation for porosity of the agglomerate clusters

The porosity of the agglomerate clusters around the macropores, ε_{ac} in Eq. (2), is defined as the ratio of the volume of pores inside the mesoscale unit cell to the total volume of the mesoscale unit cell or, equivalently, one minus the ratio of the volume of solid parts of the mesoscale unit cell to the total volume of the mesoscale unit cell as follows:

$$\begin{aligned}\varepsilon_{ac} &= 1 - \frac{V_{Pt} + V_C + V_i}{V_{meu}} \\ &= 1 - \frac{n_{Pt}\frac{4}{3}\pi r_{Pt}^3 + n_C\frac{4}{3}\pi r_C^3(1-\varepsilon_C) + t_i(2A_i)}{\left[2\left(r_{agg} - \omega_{agg}\right)\right]^3}\end{aligned} \tag{B.1}$$

where n_{Pt} and n_C are the number of platinum particles and the number of carbon particles inside an agglomerate, respectively; ε_C is the porosity of each individual carbon particle; A_i is the surface of ionomer on half of the aggregate (see Eq. (10)), and ω_{agg} is the overlap depth of the aggregates (see Figs. A.1 and C.1a).

Having the relation for t_i from Eq. (D.3), the relation between n_{Pt} and n_C from Eq. (D.1), the relation for n_C from Eq. (D.4), and the geometrical relations of the aggregates from Eqs. (A.1) and (A.2), the relation for ε_{ac} becomes:

$$\begin{aligned}\varepsilon_{ac} = 1 - \pi^2(1-\varepsilon_C)&\left[1 + l_{Pt}\frac{\rho_C}{\rho_{Pt}} + \frac{\rho_C l_i(1+l_{Pt})}{\rho_i(1-l_i)}\right] \\ &\times \frac{\frac{4}{3} - \left[1-\cos\left(\frac{\theta_{agg}}{2}\right)\right]\left\{3\sin^2\left(\frac{\theta_{agg}}{2}\right) + \left[1-\cos\left(\frac{\theta_{agg}}{2}\right)\right]^2\right\}}{48\cos^3\left(\frac{\theta_{agg}}{2}\right)}\end{aligned} \tag{B.2}$$

where θ_{agg} is the overlap angle of the aggregates (see Figs. A.1 and C.1 a).

Appendix C. a general model for gas resistance between overlapping spheres

Using the Kennard's model [62], which is valid for all the continuum, temperature jump, transition, and free molecular regimes [63], conduction through a gas between two overlapping spheres with equal radii, shown in Fig. C.1 a, is obtained as:

$$Q_g = \iint_S \frac{k_g(T_{top} - T_{bot})}{D+M}\,dA \tag{C.1}$$

where M is a gas parameter (see Ref. [64] for relations of M), and S is the surface of one of the overlapping spheres. Therefore, R_g is obtained as:

$$R_g = \frac{(T_{top} - T_{bot})}{Q_g} = \frac{1}{k_g}\left[\iint_S \frac{dA}{D+M}\right]^{-1} \tag{C.2}$$

Considering that the equation for heat conduction is linear, the superposition principle can be used as the equivalence of surfaces shown in Fig. C.1 to simplify the calculation of the surface integral in Eq. (C.2), as follows:

$$R_g = \frac{1}{k_g}\left[\iint_{S_I} \frac{dA}{D+M} - \iint_{S_{II}} \frac{dA}{D+M}\right]^{-1} \tag{C.3}$$

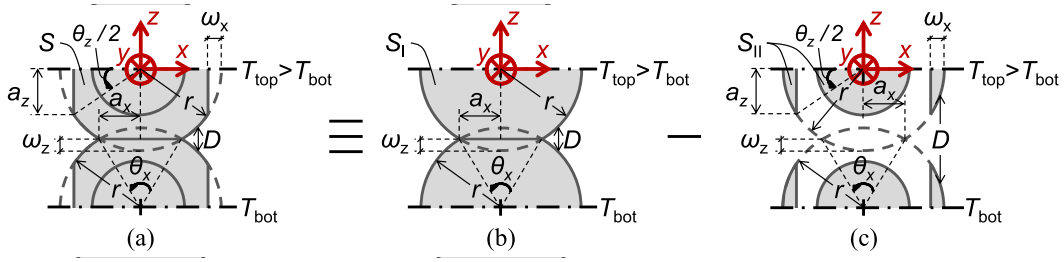

Fig. C.1. Equivalence of (a) two overlapping spheres, to (b) two overlapping spheres with the side caps, minus (c) the side caps (each sphere is overlapped with six neighboring spheres due to the considered simple cubic arrangement of the spheres in the packed bed).

After calculating the surface integrals in Eq. (C.3) based on the geometries shown in Fig. C.1, the gas resistance is obtained as:

where $\eta = r - \omega_z + M/2$.

$$R_g = \frac{1}{k_g}\left[\pi r \ln\left(\frac{\eta}{\eta - r\cos(\theta_x/2)}\right) - 2\pi r \times \left\{\frac{2\eta}{\sqrt{\eta^2 - r^2}}\left[\tan^{-1}\left(\frac{r}{\sqrt{\eta^2 - r^2}}\right) - \tan^{-1}\left(\frac{r - \eta\tan(\theta_z/4)}{\sqrt{\eta^2 - r^2}}\right)\right] - \frac{\theta_z}{2}\right\}\right]^{-1} \quad (C.4)$$

Appendix D. derivation of the relation for thickness of the ionomer film around the aggregates

The relation for the ionomer thickness, t_i in Eq. (9), is obtained from the composition of the catalyst layer defined by its platinum loading and ionomer loading. The platinum loading, denoted by l_{Pt}, and the ionomer loading, denoted by l_i, are defined as:

$$l_{Pt} = \frac{m_{Pt}}{m_C} = \frac{\rho_{Pt} n_{Pt} \frac{4}{3}\pi r_{Pt}^3}{\rho_C n_C \frac{4}{3}\pi r_C^3 (1-\varepsilon_C)} = \left(\frac{1}{1-\varepsilon_C}\right)\left(\frac{\rho_{Pt}}{\rho_C}\right)\left(\frac{n_{Pt}}{n_C}\right)\left(\frac{r_{Pt}}{r_C}\right)^3 \quad (D.1)$$

$$l_i = \frac{m_i}{m_i + m_{Pt} + m_C} = \frac{\rho_i t_i (2A_i)}{\rho_i t_i (2A_i) + \rho_{Pt} n_{Pt} \frac{4}{3}\pi r_{Pt}^3 + \rho_C n_C \frac{4}{3}\pi r_C^3 (1-\varepsilon_C)} \quad (D.2)$$

where n_{Pt} and n_C are the number of platinum particles and the number of carbon particles in the aggregate, respectively, and ε_C is the porosity of each individual carbon particle. By combining Eqs. (D.1) and (D.2), the following relation is obtained for t_i:

$$t_i = \frac{4\pi\rho_C n_C r_C^3 l_i (1 + l_{Pt})(1-\varepsilon_C)}{3\rho_i (2A_i)(1 - l_i)} \quad (D.3)$$

where n_C can be obtained by dividing the volume of the aggregate by the volume of a microscale unit cell, as follows:

$$n_C = \frac{\frac{4}{3}\pi r_{agg}^3 - V_{oa}}{V_{miu}} = \frac{\frac{4}{3}\pi r_{agg}^3 - \frac{\pi}{6}\omega_{agg}\left(3a_{agg}^2 + \omega_{agg}^2\right) \times 6}{(2r_C)^3} \quad (D.4)$$

Appendix E. derivation of the relation for constriction or spreading resistance of the Pt/C aggregate

Considering a differential slab element between two infinitely close isotherms (see Fig. 3), spreading or constriction resistance of the aggregate can be found by integration as follows:

$$R_{con,agg} = R_{spr,agg} = \int_{z=0}^{z=r_{agg}-\omega_{agg}} dR_{agg} \quad (E.1)$$

As shown in Fig. 3, the area inside the aggregate can be divided into two parts: i) overlapping area, and ii) non-overlapping area. Accordingly, for convenience, the integral in Eq. (E.1) can be divided into respective parts for the overlapping and non-overlapping areas, as follows:

$$R_{con,agg} = R_{spr,agg} = R_{agg,noa} + R_{agg,oa} \quad (E.2)$$

where $R_{agg,noa}$ and $R_{agg,oa}$ are the resistances of half of the aggregate inside the non-overlapping area and overlapping area, respectively, and are defined by:

$$R_{agg,noa} = \int_{z=a_{agg}}^{z=r_{agg}-\omega_{agg}} dR_{agg,noa} \quad (E.3)$$

$$R_{agg,oa} = \int_{z=0}^{z=a_{agg}} dR_{agg,oa} \quad (E.4)$$

where the differential resistances $dR_{agg,noa}$ and $dR_{agg,oa}$ are obtained from:

$$dR_{agg,noa} = \frac{dz}{k_{agg} A_{noa}} \quad (E.5)$$

$$dR_{agg,oa} = \frac{dz}{k_{agg} A_{oa}} \quad (E.6)$$

where A_{noa} and A_{oa} are the cross sectional areas of the aggregate in the non-overlapping area and overlapping area, respectively, and are obtained from:

$$A_{noa} = \pi\left(r_{agg}^2 - z^2\right) \quad (E.7)$$

$$A_{oa} = \pi\left(r_{agg}^2 - z^2\right) - 4A_{cs} \quad (E.8)$$

where A_{cs} , shown in Fig. E.1, is the cross sectional area inside one of

the four sideways cut cap segments of the aggregate. Using the geometry shown in Fig. E.1, A_{cs} is obtained from:

$$A_{cs} = \int_{r_{agg}-\omega_{agg}}^{\sqrt{r_{agg}^2-z^2}} \int_{-\sqrt{r_{agg}^2-y^2-z^2}}^{\sqrt{r_{agg}^2-y^2-z^2}} dxdy$$
$$= -\left(r_{agg}-\omega_{agg}\right)\sqrt{r_{agg}^2-\left(r_{agg}-\omega_{agg}\right)^2-z^2} + \left(r_{agg}^2-z^2\right) \times \left(\frac{\pi}{2} - \tan^{-1}\left(\frac{r_{agg}-\omega_{agg}}{\sqrt{r_{agg}^2-\left(r_{agg}-\omega_{agg}\right)^2-z^2}}\right)\right) \quad \text{(E.9)}$$

By combining Eqs. (E.3), (E.5), and (E.7) together and Eqs. (E.4), (E.6), (E.8), and (E.9) together, the following relations are obtained for $R_{agg,noa}$ and $R_{agg,oa}$:

$$R_{agg,noa} = \frac{1}{2\pi k_{agg} r_{agg}} \ln\left(\frac{\left(2r_{agg}-\omega_{agg}\right)\left(r_{agg}-a_{agg}\right)}{\omega_{agg}\left(r_{agg}+a_{agg}\right)}\right) \quad \text{(E.10)}$$

$$R_{agg,oa} = \frac{1}{k_{agg}} \times \int_0^{a_{agg}} \frac{dz}{\left(\begin{array}{c} -\pi\left(r_{agg}^2-z^2\right)+4\left(r_{agg}-\omega_{agg}\right)\sqrt{r_{agg}^2-\left(r_{agg}-\omega_{agg}\right)^2-z^2} \\ +4\left(r_{agg}^2-z^2\right)\tan^{-1}\left(\frac{r_{agg}-\omega_{agg}}{\sqrt{r_{agg}^2-\left(r_{agg}-\omega_{agg}\right)^2-z^2}}\right) \end{array}\right)} \quad \text{(E.11)}$$

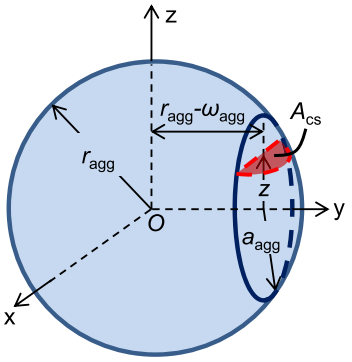

Fig. E.1. Cross sectional area inside one of the four sideways cut cap segments of the Pt/C aggregate.

References

[1] M.J. Lampinen, M. Fomino, Analysis of free energy and entropy changes for half-cell reactions, J. Electrochem. Soc. 140 (1993) 3537–3546.
[2] S.G. Kandlikar, Z. Lu, Thermal management issues in a PEMFC stack-a brief review of current status, Appl. Therm. Eng. 29 (2009) 1276–1280.
[3] M. Khandelwal, M.M. Mench, Direct measurement of through-plane thermal conductivity and contact resistance in fuel cell materials, J. Power Sources 161 (2006) 1106–1115.
[4] M. Bhaiya, A. Putz, M. Secanell, Analysis of non-isothermal effects on polymer electrolyte fuel cell electrode assemblies, Electrochim. Acta 147 (2014) 294–309.
[5] J. Wu, X.Z. Yuan, J.J. Martin, H. Wang, J. Zhang, J. Shen, S. Wu, W. Merida, A review of PEM fuel cell durability: degradation mechanisms and mitigation strategies, J. Power Sources 184 (2008) 104–119.
[6] K. Jiao, X. Li, Cold start analysis of polymer electrolyte membrane fuel cells, Int. J. Hydrogen Energy 35 (2010) 5077–5094.
[7] K. Jiao, X. Li, Effects of various operating and initial conditions on cold start performance of polymer electrolyte membrane fuel cells, Int. J. Hydrogen Energy 34 (2009) 8171–8184.
[8] K. Jiao, X. Li, Three-dimensional multiphase modeling of cold start processes in polymer electrolyte membrane fuel cells, Electrochim. Acta 54 (2009) 6876–6891.
[9] M. Khandelwal, S. Lee, M.M. Mench, One-dimensional thermal model of cold-start in a polymer electrolyte fuel cell stack, J. Power Sources 172 (2007) 816–830.
[10] J. Yuan, B. Sundén, On continuum models for heat transfer in micro/nano-scale porous structures relevant for fuel cells, Int. J. Heat Mass Transf. 58 (2013) 441–456.
[11] O.S. Burheim, H. Su, H.H. Hauge, S. Pasupathi, B.G. Pollet, Study of thermal conductivity of PEM fuel cell catalyst layers, Int. J. Hydrogen Energy 39 (2014) 9397–9408.
[12] E. Sadeghi, M. Bahrami, N. Djilali, Analytic determination of the effective thermal conductivity of PEM fuel cell gas diffusion layers, J. Power Sources 179 (2008) 200–208.
[13] J. Ramousse, S. Didierjean, O. Lottin, D. Maillet, Estimation of the effective thermal conductivity of carbon felts used as PEMFC gas diffusion layers, Int. J. Therm. Sci. 47 (2008) 1–6.
[14] E. Sadeghi, N. Djilali, M. Bahrami, Effective thermal conductivity and thermal contact resistance of gas diffusion layers in proton exchange membrane fuel cells. Part 2: Hysteresis effect under cyclic compressive load, J. Power Sources 195 (2010) 8104–8109.
[15] O. Burheim, P.J.S. Vie, J.G. Pharoah, S. Kjelstrup, Ex situ measurements of through-plane thermal conductivities in a polymer electrolyte fuel cell, J. Power Sources 195 (2010) 249–256.
[16] G. Karimi, X. Li, P. Teertstra, Measurement of through-plane effective thermal conductivity and contact resistance in PEM fuel cell diffusion media, Electrochim. Acta 55 (2010) 1619–1625.
[17] E. Sadeghi, N. Djilali, M. Bahrami, Effective thermal conductivity and thermal contact resistance of gas diffusion layers in proton exchange membrane fuel cells. Part 1: effect of compressive load, J. Power Sources 196 (2011) 246–254.
[18] E. Sadeghi, N. Djilali, M. Bahrami, A novel approach to determine the in-plane thermal conductivity of gas diffusion layers in proton exchange membrane fuel cells, J. Power Sources 196 (2011) 3565–3571.
[19] N. Zamel, E. Litovsky, S. Shakhshir, X. Li, J. Kleiman, Measurement of in-plane thermal conductivity of carbon paper diffusion media in the temperature range of -20C to +120°C, Appl. Energy 88 (2011) 3042–3050.
[20] O.S. Burheim, J.G. Pharoah, H. Lampert, P.J.S. Vie, S. Kjelstrup, Through-plane thermal conductivity of PEMFC porous transport layers, J. Fuel Cell Sci. Technol. 8 (2011) 021013-1–021013-11.
[21] H. Sadeghifar, M. Bahrami, N. Djilali, A statistically-based thermal conductivity model for fuel cell gas diffusion layers, J. Power Sources 233 (2013) 369–379.
[22] N. Zamel, X. Li, Effective transport properties for polymer electrolyte membrane fuel cells – with a focus on the gas diffusion layer, Prog. Energy Combust. Sci. 39 (2013) 111–146.
[23] O.S. Burheim, G. Ellila, J.D. Fairweather, A. Labouriau, S. Kjelstrup, J.G. Pharoah, Ageing and thermal conductivity of porous transport layers used for PEM fuel cells, J. Power Sources 221 (2013) 356–365.
[24] N. Alhazmi, M.S. Ismail, D.B. Ingham, K.J. Hughes, L. Ma, M. Pourkashanian, The in-plane thermal conductivity and the contact resistance of the components of the membrane electrode assembly in proton exchange membrane fuel cells, J. Power Sources 241 (2013) 136–145.
[25] N. Alhazmi, D.B. Ingham, M.S. Ismail, K. Hughes, L. Ma, M. Pourkashanian, The through-plane thermal conductivity and the contact resistance of the components of the membrane electrode assembly and gas diffusion layer in proton exchange membrane fuel cells, J. Power Sources 270 (2014) 59–67.
[26] H. Sadeghifar, N. Djilali, M. Bahrami, Effect of Polytetrafluoroethylene (PTFE) and micro porous layer (MPL) on thermal conductivity of fuel cell gas diffusion layers: modeling and experiments, J. Power Sources 248 (2014) 632–641.
[27] M. Ahadi, M. Andisheh-Tadbir, M. Tam, M. Bahrami, An improved transient plane source method for measuring thermal conductivity of thin films: deconvoluting thermal contact resistance, Int. J. Heat Mass Transf. 96 (2016) 371–380.
[28] N. Zamel, J. Becker, A. Wiegmann, Estimating the thermal conductivity and diffusion coefficient of the microporous layer of polymer electrolyte membrane fuel cells, J. Power Sources 207 (2012) 70–80.
[29] G. Unsworth, N. Zamel, X. Li, Through-plane thermal conductivity of the microporous layer in a polymer electrolyte membrane fuel cell, Int. J. Hydrogen Energy 37 (2012) 5161–5169.
[30] O.S. Burheim, H. Su, S. Pasupathi, J.G. Pharoah, B.G. Pollet, Thermal conductivity and temperature profiles of the micro porous layers used for the polymer electrolyte membrane fuel cell, Int. J. Hydrogen Energy 38 (2013) 8437–8447.
[31] A. Thomas, G. Maranzana, S. Didierjean, J. Dillet, O. Lottin, Thermal and water transfer in PEMFCs: investigating the role of the microporous layer, Int. J. Hydrogen Energy 39 (2014) 2649–2658.
[32] M. Andisheh-Tadbir, E. Kjeang, M. Bahrami, Thermal conductivity of microporous layers: analytical modeling and experimental validation, J. Power Sources 296 (2015) 344–351.
[33] M. Ahadi, M. Tam, M.S. Saha, J. Stumper, M. Bahrami, Thermal conductivity of catalyst layer of polymer electrolyte membrane fuel cells: Part 1 – experimental study, J. Power Sources 354 (2017) 207–214.
[34] K.L. More, R. Borup, K.S. Reeves, Identifying contributing degradation phenomena in PEM fuel cell membrane electrode assemblies via electron microscopy, ECS Trans. 3 (2006) 717–733.
[35] K. Malek, M. Eikerling, Q. Wang, T. Navessin, Z. Liu, Self-organization in catalyst layers of polymer electrolyte fuel cells, J. Phys. Chem. C 111 (2007)

13627–13634.
[36] T.E. Springer, T.A. Zawodzinski, S. Gottesfeld, Polymer electrolyte fuel cell model, J. Electrochem. Soc. 138 (1991) 2334–2342.
[37] T.E. Springer, M.S. Wilson, S. Gottesfeld, Modeling and experimental diagnostics in polymer electrolyte fuel cells, J. Electrochem. Soc. 140 (1993) 3513–3526.
[38] C. Marr, X. Li, Composition and performance modelling of catalyst layer in a proton exchange membrane fuel cell, J. Power Sources 77 (1999) 17–27.
[39] W. Sun, B.A. Peppley, K. Karan, An improved two-dimensional agglomerate cathode model to study the influence of catalyst layer structural parameters, Electrochim. Acta 50 (2005) 3359–3374.
[40] M. Srinivasarao, D. Bhattacharyya, R. Rengaswamy, S. Narasimhan, Performance analysis of a PEM fuel cell cathode with multiple catalyst layers, Int. J. Hydrogen Energy 35 (2010) 6356–6365.
[41] E. Sadeghi, A. Putz, M. Eikerling, Hierarchical model of reaction rate distributions and effectiveness factors in catalyst layers of polymer electrolyte fuel cells, J. Electrochem. Soc. 160 (2013) F1159–F1169.
[42] M. Moore, P. Wardlaw, P. Dobson, J.J. Boisvert, A. Putz, R.J. Spiteri, M. Secanell, Understanding the effect of kinetic and mass transport processes in cathode agglomerates, J. Electrochem. Soc. 161 (2014) E3125–E3137.
[43] K.J. Lange, P.C. Sui, N. Djilali, Pore scale simulation of transport and electrochemical reactions in reconstructed PEMFC catalyst layers, J. Electrochem. Soc. 157 (2010) B1434–B1442.
[44] N.A. Siddique, F. Liu, Process based reconstruction and simulation of a three-dimensional fuel cell catalyst layer, Electrochim. Acta 55 (2010) 5357–5366.
[45] C. Ziegler, S. Thiele, R. Zengerle, Direct three-dimensional reconstruction of a nanoporous catalyst layer for a polymer electrolyte fuel cell, J. Power Sources 196 (2011) 2094–2097.
[46] T. Sobolyeva, On the Microstructure of Pem Fuel Cell Catalyst Layers, Ph.D. thesis, Science: Department of Chemistry, Simon Fraser University, 2010.
[47] T. Soboleva, X. Zhao, K. Malek, Z. Xie, T. Navessin, S. Holdcroft, On the micro-, meso-, and macroporous structures of polymer electrolyte membrane fuel cell catalyst layers, ACS Appl. Mater. Interfaces 2 (2010) 375–384.
[48] S. Holdcroft, Fuel cell catalyst layers: a polymer science perspective, Chem. Mater. 26 (2014) 381–393.
[49] H.S. Carslaw, J.C. Jaeger, Conduction of Heat in Solids, second ed., Clarendon Press, Oxford, 1959.
[50] M. Bahrami, M.M. Yovanovich, J.R. Culham, Thermal joint resistances of nonconforming rough surfaces with gas-filled gaps, J. Thermophys. Heat Transf. 18 (2004) 326–332.
[51] M. Wang, N. Pan, Predictions of effective physical properties of complex multiphase materials, Mater. Sci. Eng. R 63 (2008) 1–30.
[52] K.L. Johnson, Contact Mechanics, Cambridge University Press, Cambridge, 1985.
[53] D. Guo, G. Xie, J. Luo, Mechanical properties of nanoparticles: basics and applications, J. Phys. D Appl. Phys. 47 (2014) 013001, http://dx.doi.org/10.1088/0022-3727/47/1/013001.
[54] K.L. Johnson, K. Kendall, A.D. Roberts, Surface energy and the contact of elastic solids, P. Roy. Soc. Lond. A Mater. 324 (1971) 301–313.
[55] B.V. Derjaguin, V.M. Muller, Y.P. Toporov, Effect of contact deformations on the adhesion of particles, J. Colloid Interface Sci. 53 (1975) 314–326.
[56] D. Tabor, Surface forces and surface interactions, J. Colloid Interface Sci. 58 (1977) 2–13.
[57] A. Bejan, A.D. Kraus, Heat Transfer Handbook, John Wiley & Sons, Inc., Hoboken, 2003, pp. 274–275.
[58] J. Ordonez-Miranda, R. Yang, S. Volz, J.J. Alvarado-Gil, Steady state and modulated heat conduction in layered systems predicted by the analytical solution of the phonon Boltzmann transport equation, J. Appl. Phys. 118 (2015) 075103, http://dx.doi.org/10.1063/1.4928770.
[59] M. Ahadi, M. Andisheh-Tadbir, M. Tam, M. Bahrami, An improved transient plane source method for measuring thermal conductivity of thin films: deconvoluting thermal contact resistance, Int. J. Heat Mass Transf. 96 (2016) 371–380.
[60] A. Voet, P. Aboytes, Porosity of carbon blacks, Carbon 9 (1971) 135–138.
[61] E. Sadeghi, A. Putz, M. Eikerling, Effects of ionomer coverage on agglomerate effectiveness in catalyst layers of polymer electrolyte fuel cells, J. Solid State Electrochem. 18 (2014) 1271–1279.
[62] E.H. Kennard, Kinetic Theory of Gases: with an Introduction to Statistical Mechanics, McGraw–Hill, New York, 1938.
[63] M.M. Yovanovich, Thermal contact correlations, american institute of aeronautics and astronautics, in: Thermophysics Conference, 16th, Palo Alto, CA, June 23-25, 1981, Paper 81 -1164, in: Spacecraft Radiative Transfer and Temperature Control. (A82-89949 20-18) New York, American Institute of Aeronautics and Astronautics, 1982, pp. 83–95.
[64] M. Bahrami, M.M. Yovanovich, J.R. Culham, Thermal joint resistances of conforming rough surfaces with gas-filled gaps, J. Thermophys. Heat. Tr. 18 (2004) 318–325.